Journal of
Materials Chemistry A

Accepted Manuscript

Journal of
Materials Chemistry A

Materials for energy and sustainability
www.rsc.org/MaterialsA

Volume 4 | Number 1 | 7 January 2016 | Pages 1–330

ISSN 2050-7488

ROYAL SOCIETY OF CHEMISTRY

PAPER
Kun Chang, Zhaorong Chang et al.
Bubble-template-assisted synthesis of hollow fullerene-like
MoS₂ nanocages as a lithium ion battery anode material

175 YEARS

This is an Accepted Manuscript, which has been through the Royal Society of Chemistry peer review process and has been accepted for publication.

Accepted Manuscripts are published online shortly after acceptance, before technical editing, formatting and proof reading. Using this free service, authors can make their results available to the community, in citable form, before we publish the edited article. We will replace this Accepted Manuscript with the edited and formatted Advance Article as soon as it is available.

You can find more information about Accepted Manuscripts in the author guidelines.

Please note that technical editing may introduce minor changes to the text and/or graphics, which may alter content. The journal's standard Terms & Conditions and the ethical guidelines, outlined in our author and reviewer resource centre, still apply. In no event shall the Royal Society of Chemistry be held responsible for any errors or omissions in this Accepted Manuscript or any consequences arising from the use of any information it contains.

ROYAL SOCIETY OF CHEMISTRY

rsc.li/materials-a

Journal Name

ARTICLE

Achieving Highly Stable Li-O₂ Battery Operations by Designing Carbon Nitride-Based Cathode towards Stable Reaction Interface

Peili Lou,[a,b] Zhonghui Cui[a,*] and Xiangxin Guo[a,*]

The aprotic Li-O₂ batteries have attracted a great deal of attention for their potential to offer much higher energy density than that provided by commercialized lithium-ion batteries. However, their reversible operation is plagued by serious side-reactions from liquid electrolytes and/or carbon-based materials. Recently, carbon-free materials have been proposed and attempted to construct stable cathode for Li/O₂ chemistry. Different with most of the previously reported metal-based carbon-free cathodes, herein we report a non-metal-based carbon-free cathode support consisting of mesoporous boron-doped carbon nitride (m-BCN), and demonstrate its excellent stability and activity upon Li/O₂ chemistry. Benefited from the introduction of evenly distributed RuO_2 nanoparticles (1-2 nm) in the pore of the boron-doped carbon nitride support, excellent cycle stability with low overpotential (141 cycles with pristine Li anode and extended to 227 cycles after replacing a new Li anode at 0.5 mA cm⁻²) and rate capability (1.28 mAh cm⁻² at 1 mA cm⁻²) are obtained. This impressive performance is ascribed to the enhanced stability and activity of such designed cathodes, which is supported by the fact that the reversible formation and decomposition of Li_2O_2 but no accumulation of Li_2CO_3 is detected during cycling. These results demonstrate that manipulating cathode materials towards stable reaction interfaces is essential for alleviating the formation of by-products and improving the performance of Li-O₂ batteries.

Introduction

In recent years, identifying new energy storage systems that could enable higher energy density than that of currently commercialized lithium-ion batteries (LIBs) has been becoming the focus of battery research.[1] Accidentally introducing some oxygen into LIB brings incredible increase in discharge capacity, leading to the discovery of the aprotic lithium-oxygen (Li-O₂) battery,[2] which is able to deliver several times higher energy density than that of state-of-the-art LIBs.[2-5] The rechargeable Li-O₂ battery theoretically works based on a simple reaction of 2Li + O₂ = Li_2O_2, with Li_2O_2 as the reversible mediator formed on discharge and decomposed on recharge.[2-6] However, their reversible operation is plagued by serious side-reactions from organic electrolytes and/or carbon-based cathode materials.[5-8] For example, the decomposition of organic electrolytes and carbon-based cathode materials caused by oxygen radicals like O_2^- and O_2^{2-} incurs the formation of carbonates, LiOH and other irreversible species, leading to high overpotential, low energy efficiency and poor cyclability. This indicates that the stability of cell components is of prime importance, motivating efforts to search for stable materials that are inert to the O_2^-/O_2^{2-}.[9-11]

In regard to the cathode, carbon-free materials have been proposed to offer stable reaction interfaces for Li-O₂ chemistry.[12-26] For example, noble metals (e.g., Au,[12, 13] Ru,[14, 15] RuO_2[16]), transition metal oxides (e.g., Co_3O_4,[17] $MnCo_2O_4$,[18] Ti_4O_7[19]) and carbides (e.g., TiC[20]), composites of noble metals and transition metal compounds (e.g., RuO_2/Mn_2O_3,[21] TiO_2-nanowires@porous-RuO_2,[22] Ru/ITO,[23] $RuO_2@TiN$[24] and Au@MnO_2[25]), as well as a few non-metal compounds (e.g., B_4C[26]) have been attempted in recent years. For these reported carbon-free cathodes (hosts), one can find that almost all of them are metal-based materials, which are of high densities and will incur compromise to the energy density of their resulted Li-O₂ batteries. Comparatively, non-metal compounds consisting of elemental C, B and N are indeed with low densities; smart designs based on these materials are promising to show good battery performance. Graphitic carbon nitride (g-C_3N_4) is a typical one of non-metal compounds, which has attracted extensive attentions due to its unexpected catalytic activity for a variety of reaction.[27] With this material, a free-standing oxygen cathode consisting of mesoporous graphene@g-C_3N_4 was developed, showing very large discharge capacity and enhanced cyclability.[28] Another similar design was reported by Yi et al. who composite the g-C_3N_4 with carbon paper and demonstrate an improved battery performance.[29] Besides g-C_3N_4, a sole B_3N based cathode was designed for Li-O₂ battery, which also shown enhanced cyclability.[26] These reports imply that such non-metal based carbon-free materials have better stability against oxygen reduction/evaluation reactions (ORR/OER) than carbon materials, mainly due to the absence of fragile C-C bond. Nevertheless, the available reports concerning

a. State Key Laboratory of High Performance Ceramics and Superfine Microstructure, Shanghai Institute of Ceramics, Chinese Academy of Sciences, Shanghai, 200050 China.

b. University of Chinese Academy of Sciences, Beijing, 100039 China.

* Corresponding author: cuizhonghui@mail.sic.ac.cn (Z. Cui) or xxguo@mail.sic.ac.cn (X. Guo)

such non-metal carbon-free materials appear to be numbered. Searching for new non-metal based carbon-free materials, optimizing their structure-performance and exploring their full advantage and potential are still open for further studies.
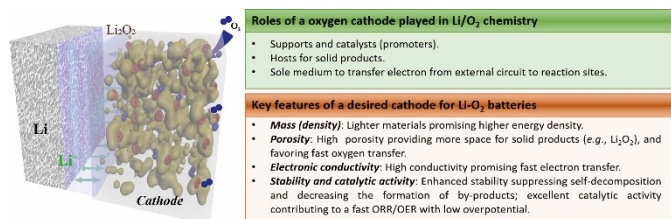

Figure 1. The key features of a desired cathode for Li-O₂ batteries.

Different with the well-known LIBs, in which the cathodes are active materials, the cathodes for Li-O₂ batteries are the places for Li/O₂ reaction, the hosts for reaction products, the mediums for electron transfer, and the catalysts or promoters for Li/O₂ reaction. Thus, several basic factors should be taken into account when searching for a suitable cathode for Li-O₂ battery (**Figure 1**): (1) *Mass (Density)* The cathodes for Li-O₂ batteries are not the active materials but rather the hosts for the reaction products of Li/O₂ chemistry, thus lighter materials providing higher specific energy densities. (2) *Porosity* The products of Li-O₂ batteries whether the desired Li_2O_2 or unwanted by-products like carbonates are solid and need to be stored within the pore of the cathodes, thus the cathode with higher porosity providing higher capacity if the supply of O₂ and Li⁺ can be maintained. (3) *Electronic conductivity* As the sole medium to allow favourable electron transport from external circuit to Li/O₂ reaction sites, the cathodes with better electronic conductivity promise more efficient and immediate supply of electrons and fast kinetics of Li/O₂ reaction. (4) *Stability and catalytic activity upon ORR/OER* As the reaction sites of Li/O₂ chemistry, the cathodes with enhanced stability and catalytic activity upon ORR/OER are of strong promise to diminish the formation of by-products and promote the formation and decomposition of Li_2O_2, leading to better battery performance. Keeping these factors in mind, in this work, we demonstrate a ruthenium oxide (RuO₂) nanoparticles decorated mesoporous boron-doped carbon nitride (RuO₂@m-BCN) composite as a stable carbon-free cathode for Li-O₂ battery. In this material, firstly, the labile "carbon" is avoided, thus promising to negate the formation of carbon-decomposition induced carbonates and the carbon catalytic effect on the electrolyte decomposition forming extra carbonates. Secondly, the evenly distributed RuO₂ nanoparticles (1-2 nm) provide abundant active sites for ORR/OER, leading to greatly enhanced catalytic effect.[30-32] Thirdly, the evenly distributed RuO₂ nanoparticles significantly improve the electronic conductivity of RuO₂@m-BCN composites, guaranteeing fast electron supply. Fourthly, more O₂ molecules can be absorbed onto the electrode surface for the existence of oxygen vacancy in the RuO₂ lattices, which provides fast oxygen supply for ORR and contributes to a good rate performance. When subjected this material to Li-O₂ batteries, improved cyclability and rate performance with high energy efficiency are characterized.

Results and Discussion

Synthesis and Characterization of the RuO₂@m-BCN.

The RuO₂@m-BCN was synthesized *via* two facile steps. Firstly, mesoporous boron-doped carbon nitrides (m-BCN) as stable cathode supports were prepared by a thermal-induced condensation of the mixture of dicyanodiamide and tetrafluoroborate-based (1-Butyl-3-methylimidazolium tetrafluoroborate, BmimBF₄) ionic liquid (IL).[33] Herein, the BmimBF₄ is employed not only as the soft template to construct porous-structured carbon nitride, but also as the source of elemental boron for heteroatom-doping the carbon nitride matrix. Secondly, the decoration of the m-BCN with RuO₂ nanoparticles was completed *via* a simple solution process, in which the positive charged Ru³⁺ ions were first immobilized onto the surface of the m-BCN supports for the electrostatic interaction, and then *in situ* transformed into RuO₂ nanoparticles and embedded on the surface of m-BCN supports when introducing the NaBH₄ into the solution.
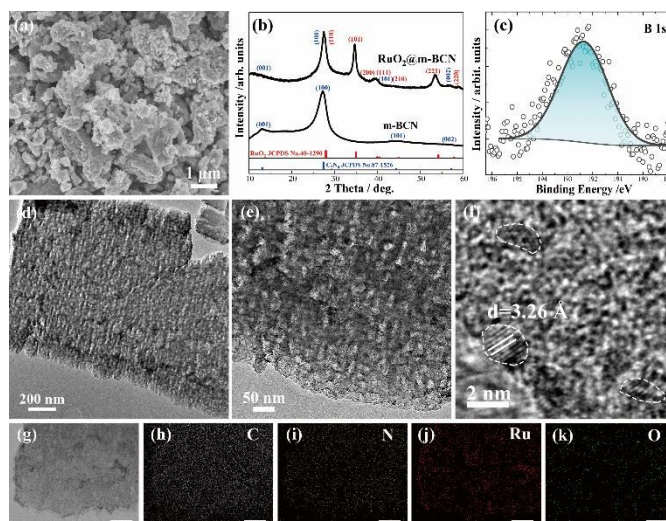

Figure 2. Structure and morphology of the as-prepared RuO₂@m-BCN. (a) SEM, (b) XRD, (c) B 1s, (d-e) TEM, (f) HRTEM, (g) STEM, and (h-k) corresponding EDS mapping of C, N, Ru and O, respectively. The scale bars in Figure 2g-k are equivalent to 100 nm.

The structure and morphology of as-prepared RuO₂@m-BCN composites were investigated by X-ray diffraction (XRD), scanning electron microscopy (SEM), transmission electron microscopy (TEM) and X-ray photoelectron spectroscopy (XPS). The SEM image indicates that the as-prepared RuO₂@m-BCN consists of porous and non-uniform agglomerates (**Figure 2**a). The porous structure is of key importance for oxygen transmission and storing of solid reaction products. Figure 2b shows the XRD patterns of the as-prepared m-BCN and RuO₂@m-BCN. The m-BCN supports show similar pattern to that of the standard graphitic carbon nitride (*g*-C₃N₄, JCPDS No. 87-1526) with two characteristic peaks arising at 13.0 and 27.4 degree, which can be indexed as the 100 peak characteristic for the interplanar separation and the 002 peak representing for the interlayer stacking of aromatic systems, respectively.[33, 34] After decorated in the RuCl₃ solution, RuO₂ (Rutile, JCPDS No.

40-1290) -like peaks appear, as shown in Figure 1a, indicating RuO_2 nanoparticles being successfully embedded onto the m-BCN supports. One can see clearly that the peaks of the as-synthesized RuO_2 slightly shift to the lower angles, which is ascribed to their non-stoichiometry feature. In order to determine the Ru/O ratio and the state of elemental doping, the XPS measurements were performed. The Ru/O ratio of the RuO_2@m-BCN is about 1.82, which is smaller than that of the perfect RuO_2 crystal. This small Ru/O ratio indicates the existence of oxygen vacancies in RuO_2 lattices, which favours the oxygen transport on the electrode surface.[24] The non-stoichiometry of the RuO_2 is further supported by the energy dispersive spectroscopy (EDS) results (Figure S1).

A peak centred at 192.4 eV is detected from the as-prepared RuO_2@m-BCN (Figure 2c), which is consistent well with the binding energy of the C-NB group,[35, 36] indicating the element boron being successfully incorporated into the g-C_3N_4 lattices. The content of boron is determined to be 4.34 mol %. B enters the C_3N_4 lattices by replacing the C-atoms forming a π-bonded, planar layered configuration and acts as electron acceptor because it has three valence electrons, inducing surface states near the valence band top and hence modifying the electronic structure of C_3N_4.[35, 36] The absence of distinct peak in the range of 680 to 696 eV reveals that no element F enters the C_3N_4 lattices (Figure S2). The mesoporous structure of the RuO_2@m-BCN and uniform decoration of the RuO_2 nanoparticles with a size of about 1-2 nm can be clearly observed from the TEM images with different magnifications (Figure 2d-f). The porous RuO_2@m-BCN offers a specific area of 136.5 $m^2 g^{-1}_{RuO_2@m-BCN}$ and a pore size distribution centred around 75 nm in the range of 11-125 nm, which is obtained from the nitrogen absorption-desorption isotherms (Figure S3). The substantial mesopores and macropores within the RuO_2@m-BCN composites favour rapid transport of the electrolyte and O_2, thus leading to an enhanced rate capability of the Li–O_2 batteries. The crystalline nature of the RuO_2 nanoparticles is confirmed by the appearance of identifiable lattice fringes in HRTEM (Figure 2f and S4). From Figure 2f, a spacing of 3.26 Å can be identified clearly from a marked particle, which is slightly larger than the spacing of the (110) plane of standard RuO_2 nanocrystals (3.18 Å). This larger interplanar spacing observed here is consistent with the results indicated from the XRD pattern that shifts to lower angles (Figure 2b). Furthermore, the high-angle annular dark field (HADAF) image and the corresponding EDS elemental mappings confirm the uniform distribution of the RuO_2 nanoparticles on the m-BCN supports (Figure 2g-k).

As discussed in Introduction, the conductivity is of important influence on the performance of Li-O_2 batteries. The electrical conductivity of the RuO_2@m-BCN and m-BCN were characterized by I-V measurement. The testing samples were prepared by pressing their powders into ~ 1 mm-thick pallet (8 mm in diameter) under a pressure of 6 MPa (Figure S5). Figure S6 shows the I-V plots of the RuO_2@m-BCN and m-BCN under a given voltage. For the m-BCN, its resistance is so high that only a very small value of current feedback can be collected. In contrast, a much larger value of current collected for RuO_2@m-BCN, indicating a significantly improved conductivity for the introduction of evenly distributed RuO_2 nanoparticles. The conductance value of RuO_2@m-BCN and m-BCN can be determined from the slope of I-V plots. Then the conductivity of the RuO_2@m-BCN and m-BCN are calculated to be 11.7 and 5.8 $\times 10^{-7}$ S cm^{-1}, respectively. This value is much lower than that of bulk RuO_2 (~ 10^4 S cm^{-1})[37] and two-dimensional RuO_2 nanosheets (~ 10^3 S cm^{-1})[16], owing to the existence of the insulator component of m-BCN and voids between every RuO_2@m-BCN particles. However, this value is comparable with that of previously reported cathodes like Co_3O_4 nanofibers immobilized on nonoxidized graphene nanoflakes[38] and metallic Magnéli phase Ti_4O_7[19], both of which provide good cyclability and large capacities. This means that the electrical conductivity of the RuO_2@m-BCN is sufficient to afford fast electron transport for the formation and decomposition of desired Li_2O_2.

Electrochemical Performance Characterization in Li-O_2 Batteries.

The electrochemical performance of the RuO_2@m-BCN composites was examined by Swagelok-type Li-O_2 batteries using 0.5 M $LiClO_4$ dissolved in dimethyl sulfoxide (DMSO) as the electrolyte. The use of $LiClO_4$/DMSO-based electrolytes is because their excellent stability upon ORR/OER, guaranteeing the formation of Li_2O_2 even for hundreds of cycles.[12] **Figure 3**a shows the initial discharge-charge profile of the RuO_2@m-BCN and m-BCN at a current density of 0.2 mA cm^{-2}. Note that there are two testing protocols present for evaluating electrode performance: the voltage-limited and capacity-limited method. Herein the voltage-limited protocol is adopted, because it favours the exploration of the full potential of a new electrode. In addition, the discharge cut-off was elaborately set at 2.5 V to avoid the lithium intercalation into the RuO_2 lattices.[39] As shown in Figure 3a, for the bare m-BCN, only a small capacity is delivered during initial discharge, while a large capacity with a voltage plateau at 4.44 V is obtained during recharge. It is noteworthy that the RuO_2@m-BCN/$LiClO_4$-DMSO has excellent electrochemical stability in a wide voltage window of 2.5- 4.5 V, which is supported by the absence of the obvious current peak in cyclic voltammetry (CV) collected under Ar atmosphere (Figure 3b). These results indicate that some oxygen radical induced side-reactions occurred at this voltage, meaning that the upper cut-off for the DMSO/m-BCN-based system should lower than the voltage of 4.44 V. In contrast, the RuO_2@m-BCN shows a well-defined plateau at 2.78 V on initial discharge and a slope ranging from 3 to 3.48 and a plateau at 3.55 followed by an upward slope at around 4 V on recharge (Figure 3a). This leads to a much larger discharge capacity as well as smaller overpotential than that of the sole m-BCN cathode (Figure 3a), indicating an enhanced activity upon ORR/OER. Specifically, the discharge capacity of the RuO_2@m-BCN increases more than 12 times to 2.57 mAh cm^{-2} (*i.e.*, 512 mAh g^{-1} based on the mass loading of the RuO_2@m-BCN), which is indeed beneficial from the highly porous structure of RuO_2@m-BCN that favours the storage of more discharge products and fast mass transport. This tailored porous structure of RuO_2@m-BCN significantly increases the contact areas between RuO_2 catalysts and discharge products, thus lowering the overpotentials to 0.18 V

for discharge and 0.54 V for recharge. Herein the discharge capacity for the RuO$_2$@m-BCN is smaller than that of many carbon-based electrodes,[10, 40] but is comparable with that of previously reported carbon-free cathodes (Table S1).[12, 19, 20, 23, 26]
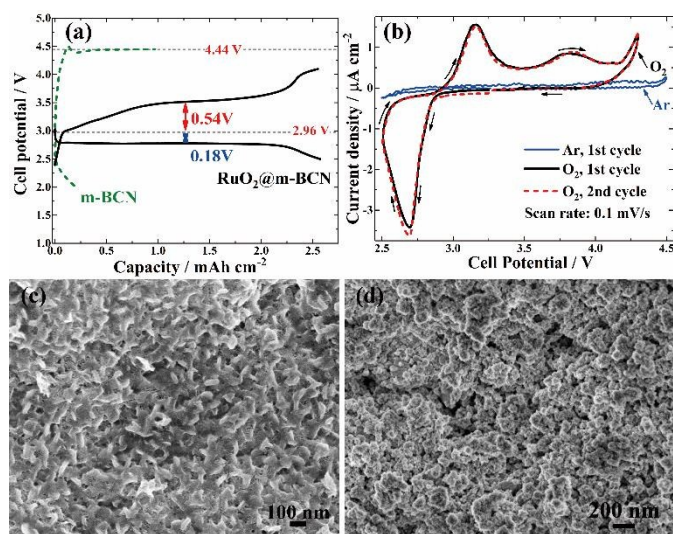

Figure 3. (a) The first discharge-charge profiles of the m-BCN and the RuO$_2$@m-BCN cathode with a current density of 0.2 mA cm^{-2}; (b) CV curves of RuO$_2$@m-BCN collected under Ar and O$_2$ saturated DMSO electrolytes, respectively; (c-d) the morphology of the 1st discharged and recharged electrode of the RuO$_2$@m-BCN, respectively.

Figure 3b shows the CV curve of the RuO$_2$@m-BCN collected in oxygen saturated DMSO electrolytes. During the first cathodic scan, one profound reduction peak appears at around 2.72 V, which corresponds to the formation of Li$_2$O$_2$. Upon anodic scan, the oxidation of discharge products gives an obvious OER peak at 3.16 V followed by a flat peak at around 3.8 V, which is well consistent with the two oxidation plateaus appeared in Figure 3a and previous reports.[19, 23, 30] It can be seen that the first oxidation peak contributes more than the second one to the total oxidation current, meaning that most of the discharge products are oxidized below 3.8 V. This indicates that the RuO$_2$@m-BCN can promote the early decomposition of Li$_2$O$_2$. For the second cycle, the CV curve remains unchanged, indicating good stability and activity of the RuO$_2$@m-BCN upon repeated ORR/OER. Besides the two oxidation peaks located at 3.16 and 3.8 V, an oxidation peak appears around the voltage cap of 4.3 V, which is attributed to the decomposition of DMSO solvents and/or some by-products.[41, 42]

During initial cycling, the morphology of the discharge products deposited on the RuO$_2$@m-BCN electrodes were visualized by SEM (Figure 3c-d). Compared with the pristine electrode (Figure S7), toroid particles meeting the characteristic morphology of Li$_2$O$_2$[6, 43, 44] with a size around 200 nm formed and fill the RuO$_2$@m-BCN cathode during initial discharge (Figure 3c). Excellent uniformity of such discharge products is further confirmed by a SEM image with lower magnification (Figure S8). The toroidal morphology indicates a solution growth mechanism of Li$_2$O$_2$ formation, which has been well studied

previously, and favour a large discharge capacity.[5, 43-48] Here, the formation of Li$_2$O$_2$ toroid may benefit from the non-stoichiometric feature of RuO$_2$ along with the contribution form DMSO-based electrolytes.[5, 24] After recharge, these discharge products are completely removed even the voltage just above 4 V (Figure 3d). These reversible morphology changes indicate the superior ability of RuO$_2$@m-BCN to promote the decomposition of discharge products during cycling, which is essential for the stable operation of Li-O$_2$ batteries.
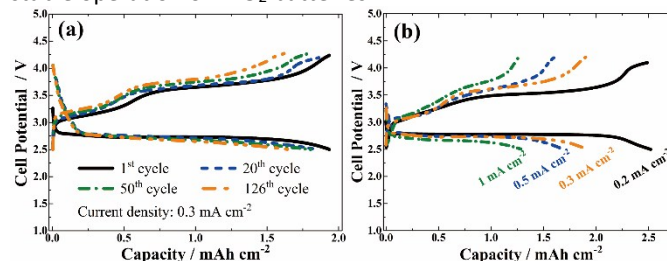

Figure 4. Electrochemical behaviour of RuO$_2$@m-BCN in Li-O$_2$ batteries. (a) cycle performance with a current density of 0.3 mA cm^{-2} and (b) rate performance.

The cyclability of the RuO$_2$@m-BCN cathodes were investigated in a full discharge-charge protocol between 2.5 and 4.2 V. Remarkably, the RuO$_2$@m-BCN cathode exhibits an impressive cycle stability up to 126-cycle with almost overlapped discharge-charge curves and stable reversible capacities around 1.8 mAh cm^{-2} at 0.3 mA cm^{-2} (Figure 4a and S9). In the course of cycling, the overpotentials for the RuO$_2$@m-BCN remain stable with a low value of ~ 0.6 V, which is completely different with the phenomenon that the overpotential increases rapidly upon cycling observed in many carbon electrodes.[10, 11, 43, 44, 47, 48] Furthermore, discharging/charging tests of this RuO$_2$@m-BCN cathode at a series of rates clearly show its superior rate capability. As shown in Figure 4b, the RuO$_2$@m-BCN deliver a reversible capacity of 1.90, 1.68, and 1.28 mAh cm^{-2} at the current density of 0.3, 0.5 and 1 mA cm^{-2}, respectively. The excellent performance of RuO$_2$@m-BCN is ascribed to the following advantages: (1) the use of m-BCN, which excludes the fragile C-C bond and thus enhances the structure stability upon cycling; (2) the introduction of evenly distributed RuO$_2$ nanoparticles, which provide substantial active sites for ORR/OER and significantly improved electronic wiring with discharge products; (3) the tailored porous structure, which favours good electrolyte wetting and fast O$_2$ transport.

In addition, the high performance of RuO$_2$@m-BCN, in some extent, may benefit from the cycle protocol, in which a higher charging cutoff is used. We previously found that charging vertical aligned carbon nanotubes based Li-O$_2$ cells to a slightly higher voltage favours the electrochemical splitting of discharge products more completely and renews the cathodes for subsequent discharging, leading to an improved cyclability.[49] Figure S10 and S11 show the cycle performance and CV curves collected from cells operated between 2.5 and 4 V, respectively. Compared with the results shown in Figure 4a, this cell suffers a poor cycle stability. The main cause should be the accumulation of by-products, leading to the bury of active sites and loss of electronic conductivity.[50]

Electrode Stability and Electrochemical Products Characterization.

To demonstrate the excellent stability of the RuO_2@m-BCN and the reversibility of formation and oxidation of Li_2O_2, the cycled electrodes were analysed by *ex-situ* XRD, XPS and Fourier transform infrared spectroscopy (FTIR). The commercialized Li_2O_2, LiOH and Li_2CO_3 powders were used as the references for identifying the chemistry of reaction products. As shown in Figure S12, the 5th discharged and pristine electrodes show almost identical XRD patterns. The main reasons for this observation may be the absence of crystalline products or their amount too small to be detected. Then the XPS analyses, a surface sensitive technique that can detect the amorphous and/or trace products formed on electrodes, were conducted. For the Li 1s photoemission spectra of the 5th cycled electrodes, a broad peak centred at 54.7 eV meeting the binding energy of Li_2O_2[30, 51] appears upon discharge and disappears after recharge (Figure 5a). Moreover, such peak appears further even in the 20th and 40th discharged electrodes, indicating the excellent repeatability of the reaction occurred on the RuO_2@m-BCN cathodes. We cannot rule out the formation of the irreversible product of LiOH from the reversible product of Li_2O_2 only from the Li 1s photoemission spectra, due to their near-identical binding energies.[52] However, the excellent reversibility (Figure 5a) and previous demonstrated rechargeability (Figure 4) lead us to tentatively conclude that the main discharge product deposited on the RuO_2@m-BCN electrodes is Li_2O_2. This conclusion is further supported by the C 1s/Ru 3d photoemission spectra (Figure 5b), in which no obvious peaks corresponding to the CO_3^{2-} can be observed. One can see only a very small peak in the discharged electrode (*e.g.*, the 5th, 20th and 40th) at around 290 eV (Figure 5b),[30, 52] helping us rule out the serious situation of formation and accumulation of Li_2CO_3 during prolonged cycling. The absence of the serious accumulation of Li_2CO_3 during long-term cycling demonstrates the superior stability of the RuO_2@m-BCN upon Li_2O_2 and superoxide-like species. For the observed small peak of Li_2CO_3, it may result from the electrode surface contamination by limited exposure to the ambient air during XPS tests, as the peak with feature of CO_3^{2-} also appeared in the commercialized Li_2O_2 and LiOH powders (Figure 5b).
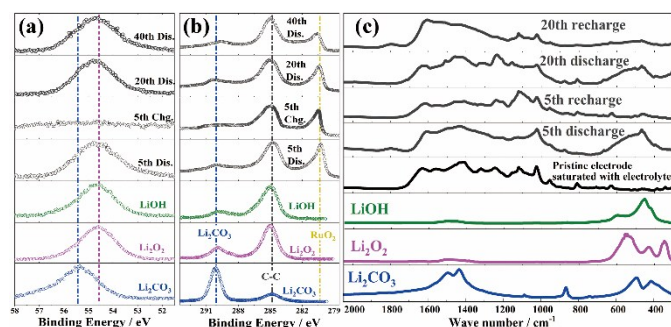

Figure 5. *Ex-situ* measurements on oxygen electrodes. *Ex-situ* XPS obtained from 5th discharged, 5th charged, 20th discharged, and 40th discharged electrodes collected in the (a) Li 1s, (b) C 1s/Ru 3d; (c) *Ex-situ* FTIR spectra obtained from

pristine, 5th discharged, 5th charged, 20th discharged, and 20th charged electrodes.

Furthermore, the cycled electrodes were investigated by *ex situ* FTIR to study whether the LiOH is involved during cycling. Compared to the spectrum of the pristine electrode saturated with DMSO-based electrolytes, a new broad peak ranging from 350 to 650 cm^{-1} appears in the 5th discharged electrode and disappears after recharge, which is also reproducible for the 20th cycle (Figure 5c). The broad characteristic peak centred at 545 cm^{-1} can be assigned to Li_2O_2, which is consist with the results from XPS (Figure 5a). Another characteristic peak appeared at 460 cm^{-1} meets the peak position of standard LiOH,[53] indicating the existence of LiOH, which has been reported several times and is ascribed to the decomposition of DMSO solvent during cycling.[54] After recharge to 4.1 V, the disappearance of this two characteristic peaks indicates that these discharge products including LiOH have been removed (Figure 5c). This results a "clear" electrode surface as showed in Figure 3d, which is crucial for subsequent operation. Here, the splitting of LiOH at around 4 V with an upward slope (Figure 4a and c) is attributed to the tailored porous structure, which guarantees the good contact of discharge products with RuO_2 catalysts.[55]
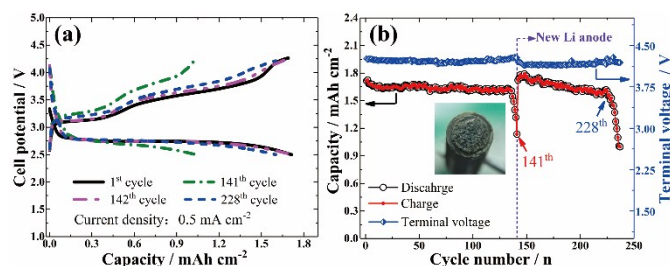

Figure 6. (a) cycle performance and (b) selected discharge-charge profiles of the RuO_2@m-BCN cathode with a current density of 0.5 mA cm^{-2}. The inset of (a) shows the photograph of the lithium anode after 141 cycles.

To further evidence the enhanced stability of this carbon-free cathode, the cell that has shown significant capacity decay after 141 cycles was reopened in the glove-box (Figure 6a). No obvious changes on cathode and electrolyte (*e.g.*, colour) can be observed by naked eye, in some extent indicating good stability. While conspicuous changes were observed in lithium anode. Specifically, the colour changes from metallic into grey; and the flat surface becomes uneven and is covered by a layer of moss-like structures (inset of Figure 6a). The same observations of the failure of Li anode were reported by Schroeder *et al.*[51] and Lu *et al.*[56]. *Ex situ* XRD analysis of another anode failed after 107 cycles indicates that the moss-like structures consist of the mixture of LiOH and Li_2O (Figure S13). The formation of such insulators significantly increase Li^+ and e^- transfer barriers, and may be the reason answering for the death of RuO_2@m-BCN based battery. To verify this, the cycled anode was replaced with a new one, and the cell was reassembled with other components unchanged. It is surprising that the reassembled cell works healthily as it behaved before the cell failure (Figure 6a-b). The cathode shows a full recovery

ARTICLE

of the cell voltage profiles and even slightly larger capacities, which last for another 87 cycles (Figure 6). The consistency in cell performance (*i.e.,* voltage profile and capacity) before and after a cycled and "dead" cell reassembled with a new lithium anode strongly suggests that the as-prepared RuO_2@m-BCN cathodes possess excellent stability and activity upon ORR/OER, guaranteeing the impressive cell performance. This also suggests that effective strategies capable of enhancing the reversibility and stability of lithium anode are urgently needed for stable operation of $Li-O_2$ batteries.

Conclusions

In summary, we developed a promising carbon-free cathode prepared by introducing RuO_2 nanoparticles into mesoporous boron doped carbon nitride (RuO_2@m-BCN). Benefitting from the evenly distributed RuO_2 and robust m-BCN, the RuO_2@m-BCN shows excellent stability and activity upon ORR/OER. With such cathodes, the $Li-O_2$ batteries demonstrate the reversible formation and decomposition of Li_2O_2 with no accumulation of Li_2CO_3, relatively low charge overpotential, excellent cycle stability and rate capability. This impressive performance is ascribed to the tailored properties of the RuO_2@m-BCN, including the inherent stability of carbon-free supports that decrease the amount of by-products from electrode and/or electrolyte self-decomposition, the enhanced catalytic activity upon Li/O_2 chemistry stemming from the evenly distributed RuO_2 nanoparticles, and the interconnected porous structures that favour the storage of more discharge products and fast mass transfer. The enhanced stability of the RuO_2@m-BCN is further supported by the consistency in voltage profiles and capacity before and after a cycled and "dead" cell reassembled with a new lithium anode. These results indicate that constructing highly efficient and stable cathode with optimized porous structure is essential for the stable operation of $Li-O_2$ batteries.

Acknowledgements

Notes and references

1   M. Armand and J. M. Tarascon, *Nature*, 2008, **451**, 652-657.
2   K. M. Abraham and Z. Jiang, *J. Electrochem. Soc.*, 1996, **143**, 1-5.
3   P. G. Bruce, S. A. Freunberger, L. J. Hardwick and J. M. Tarascon, *Nat. Mater.*, 2011, **11**, 19-29.
4   G. Girishkumar, B. McCloskey, A. C. Luntz, S. Swanson and W. Wilcke, *J. Phys. Chem. Lett.*, 2010, **1**, 2193-2203.
5   D. Aurbach, B. D. McCloskey, L. F. Nazar and P. G. Bruce, *Nat. Energy*, 2016, **1**, 16128.
6   Z. Cui, X. Guo and H. Li, *Energy Environ. Sci.*, 2015, **8**, 182-187.
7   Y. Lu, B. M. Gallant, D. G. Kwabi, J. R. Harding, R. R. Mitchell, M. S. Whittingham and Y. Shao-Horn, *Energy Environ. Sci.*, 2013, **6**, 750-768.
8   X. Yao, Q. Dong, Q. Cheng and D. Wang, *Angew. Chem. Int. Ed.*, 2016, **55**, 11344-11353.
9   M. Balaish, A. Kraytsberg and Y. Ein-Eli, *Phys. Chem. Chem. Phys.*, 2014, **16**, 2801-2822.
10 Z. Ma, X. Yuan, L. Li, Z. Ma, D. P. Wilkinson, L. Zhang and J. Zhang, *Energy Environ. Sci.*, 2015, **8**, 2144-2198.
11 Y. Shao, F. Ding, J. Xiao, J. Zhang, W. Xu, S. Park, J. Zhang, Y. Wang and J. Liu, *Adv. Funct. Mater.*, 2013, **23**, 987-1004.
12 Z. Peng, S. A. Freunberger, Y. Chen and P. G. Bruce, *Science*, 2012, **337**, 563-566.
13 S. T. Kim, N.-S. Choi, S. Park and J. Cho, *Adv. Energy Mater.*, 2015, **5**, 1401030.
14 K. Liao, T. Zhang, Y. Wang, F. Li, Z. Jian, H. Yu and H. Zhou, *ChemSusChem*, 2015, **8**, 1429-1434.
15 K.-H. Kwak, D. W. Kim, Y. Kang and J. Suk, *J. Mater. Chem. A*, 2016, **4**, 16356-16367.
16 K. Liao, X. Wang, Y. Sun, D. Tang, M. Han, P. He, X. Jiang, T. Zhang and H. Zhou, *Energy Environ. Sci.*, 2015, **8**, 1992-1997.
17 X. Han, F. Cheng, C. Chen, F. Li and J. Chen, *Inorg. Chem. Front.*, 2016, **3**, 866-871.
18 R. S. Kalubarme, H. S. Jadhav, D. T. Ngo, G. E. Park, J. G. Fisher, Y. I. Choi, W. H. Ryu and C. J. Park, *Sci. Rep.*, 2015, **5**, 13266.
19 D. Kundu, R. Black, E. J. Berg and L. F. Nazar, *Energy Environ. Sci.*, 2015, **8**, 1292-1298.
20 M. M. Ottakam Thotiyl, S. A. Freunberger, Z. Peng, Y. Chen, Z. Liu and P. G. Bruce, *Nat. Mater.*, 2013, **12**, 1050-1056.
21 K. R. Yoon, G. Y. Lee, J. W. Jung, N. H. Kim, S. O. Kim and I. D. Kim, *Nano Lett.*, 2016, **16**, 2076-2083.
22 Z. Guo, C. Li, J. Liu, X. Su, Y. Wang and Y. Xia, *J. Mater. Chem. A*, 2015, **3**, 21123-21132.
23 F. Li, D. M. Tang, Y. Chen, D. Golberg, H. Kitaura, T. Zhang, A. Yamada and H. Zhou, *Nano Lett.*, 2013, **13**, 4702-4707.
24 Y. Chang, S. Dong, Y. Ju, D. Xiao, X. Zhou, L. Zhang, X. Chen, C. Shang, L. Gu, Z. Peng and G. Cui, *Adv. Sci.*, 2015, **2**, 1500092.
25 S. Liu, G. Wang, F. Tu, J. Xie, H. Y. Yang, S. Zhang, T. Zhu, G. Cao and X. Zhao, *Nanoscale*, 2015, **7**, 9589-9596.
26 S. Song, W. Xu, R. Cao, L. Luo, M. H. Engelhard, M. E. Bowden, B. Liu, L. Estevez, C. Wang and J. Zhang, *Nano Energy*, 2017, **33**, 195-204.
27 W. J. Ong, L. L. Tan, Y. H. Ng, S. T. Yong and S. P. Chai, *Chem. Rev.*, 2016, **116**, 7159-7329.
28 W. B. Luo, S. L. Chou, J. Z. Wang, Y. C. Zhai and H. K. Liu, *Small*, 2015, **11**, 2817-2824.
29 J. Yi, K. Liao, C. Zhang, T. Zhang, F. Li and H. Zhou, *ACS Appl. Mater. Interfaces*, 2015, **7**, 10823-10827.
30 P. Lou, C. Li, Z. Cui and X. Guo, *J. Mater. Chem. A*, 2016, **4**, 241-249.
31 B. Sun, L. Guo, Y. Ju, P. Munroe, E. Wang, Z. Peng and G. Wang, *Nano Energy*, 2016, **28**, 486-494.
32 C. Zhao, C. Yu, M. N. Banis, Q. Sun, M. Zhang, X. Li, Y. Liu, Y. Zhao, H. Huang, S. Li, X. Han, B. Xiao, Z. Song, R. Li, J. Qiu and X. Sun, *Nano Energy*, 2017, **34**, 399-407.
33 Y. Wang, J. Zhang, X. Wang, M. Antonietti and H. Li, *Angew. Chem. Int. Ed.*, 2010, **49**, 3356-3359.
34 Q. Guo, Y. Xie, X. Wang, S. Lv, T. Hou and X. Liu, *Chem. Phys. Lett.*, 2003, **380**, 84-87.
35 Y. Wang, H. Li, J. Yao, X. Wang and M. Antonietti, *Chem. Sci.*, 2011, **2**, 446-450.
36 S. Zhang, L. Gao, D. Fan, X. Lv, Y. Li and Z. Yan, *Chem. Phys. Lett.*, 2017, **672**, 26-30.
37 Y. Lee, B.-U. Ye, H. k. Yu, J.-L. Lee, M. H. Kim and J. M. Baik, *J. Phys. Chem. C*, 2011, **115**, 4611-4615.
38 W. H. Ryu, T. H. Yoon, S. H. Song, S. Jeon, Y. J. Park and I. D. Kim, *Nano Lett.*, 2013, **13**, 4190-4197.

39 P. Balaya, H. Li, L. Kienle and J. Maier, *Adv. Funct. Mater.*, 2003, **13**, 621-625.

40 J. Xiao, D. Mei, X. Li, W. Xu, D. Wang, G. L. Graff, W. D. Bennett, Z. Nie, L. V. Saraf, I. A. Aksay, J. Liu and J. G. Zhang, *Nano Lett.*, 2011, **11**, 5071-5078.

41 N. Mozhzhukhina, L. P. Méndez De Leo and E. J. Calvo, *J. Phys. Chem. C*, 2013, **117**, 18375-18380.

42 M. A. Schroeder, N. Kumar, A. J. Pearse, C. Liu, S. B. Lee, G. W. Rubloff, K. Leung and M. Noked, *ACS Appl. Mater. Interfaces*, 2015, **7**, 11402-11411.

43 Z. Cui, W. Fan and X. Guo, *J. Power Sources*, 2013, **235**, 251-255.

44 W. Fan, Z. Cui and X. Guo, *J. Phys. Chem. C*, 2013, **117**, 2623-2627.

45 B. D. Adams, C. Radtke, R. Black, M. L. Trudeau, K. Zaghib and L. F. Nazar, *Energy Environ. Sci.*, 2013, **6**, 1772-1778.

46 R. R. Mitchell, B. M. Gallant, C. V. Thompson and Y. Shao-Horn, *Energy Environ. Sci.*, 2011, **4**, 2952-2958.

47 Z. Cui and X. Guo, *J. Power Sources*, 2014, **267**, 20-25.

48 T. Ogasawara, A. Débart, M. Holzapfel, P. Novák and P. G. Bruce, *J. Am. Chem. Soc.*, 2006, **128**, 1390-1393.

49 X. Guo and N. Zhao, *Adv. Energy Mater.* 2013, **3**, 1413-1416.

50 J. Wang, Y. Zhang, L. Guo, E. Wang and Z. Peng, *Angew. Chem. Int. Ed.*, 2016, **55**, 5201-5205.

51 M. A. Schroeder, A. J. Pearse, A. C. Kozen, X. Chen, K. Gregorczyk, X. Han, A. Cao, L. Hu, S. B. Lee, G. W. Rubloff and M. Noked, *Chem. Mater.*, 2015, **27**, 5305-5313.

52 Y. Lu, A. N. Mansour, N. Yabuuchi and Y. Shao-Horn, *Chem. Mater.*, 2009, **21**, 4408-4424.

53 Y. Qiao and S. Ye, *J. Phys. Chem. C*, 2016, **120**, 15830-15845.

54 D. G. Kwabi, T. P. Batcho, C. V. Amanchukwu, N. Ortiz-Vitoriano, P. Hammond, C. V. Thompson and Y. Shao-Horn, *J. Phys. Chem. Lett.*, 2014, **5**, 2850-2856.

55 F. Li, S. Wu, D. Li, T. Zhang, P. He, A. Yamada and H. Zhou, *Nat. Commun.*, 2015, **6**, 7843.

56 J. Lu, Y. J. Lee, X. Luo, K. C. Lau, M. Asadi, H. H. Wang, S. Brombosz, J. Wen, D. Zhai, Z. Chen, D. J. Miller, Y. S. Jeong, J. B. Park, Z. Z. Fang, B. Kumar, A. Salehi-Khojin, Y. K. Sun, L. A. Curtiss and K. Amine, *Nature*, 2016, **529**, 377-382.

TOC:

Key Features of a Desired Cathode for Li-O$_2$ battery

✓ Low Weight ✓ High Porosity ✓ High Conductivity ✓ Enhanced Stability and Catalytic Activity